Multiphysics data modeling and imaging for exploration in the southern Rocky Mountains

Maria Soledad Velasco[1], David Alumbaugh[1], and Emmanuel Schnetzler[1]

Abstract

We carried out a multidata geophysics study in southern Colorado to explore for CO_2 reservoirs in an area where seismic imaging is very limited due to the mountainous terrain, the presence of high-velocity volcanic rocks, and difficulty in obtaining land access permits. We have developed a modeling/interpretation methodology using ground magnetotelluric data as well as airborne magnetic and electromagnetic data combined with public domain gravity data and existing well and seismic data. We used the integration of these data sets to produce a series of 2D and 3D geophysical models that reveal basin architecture previously poorly defined through the analysis of limited seismic and well data alone. We found that this type of analysis aids in decreasing uncertainty in the interpreted geologic cross sections and a better understanding of the structural complexities of the region. Through the application of machine learning methods, we are also able to integrate several data sets into a mathematical framework resulting in a predictive model of spatial CO_2 distribution. The integration of the interpretations from all data sets, predictive analytics results, and knowledge of CO_2 production, allows us to delineate areas of interest for further exploration.

Introduction and geologic setting

The main objective of the study was to better understand the subsurface of a geologically complex region where a single geophysical method alone was unsuccessful at imaging the subsurface to help solve the problem linked to CO_2 exploration. We therefore required the use of a combination of several different geophysical methods to characterize the geology because each imaging method responds to specific rock properties that may have limited or no response to some techniques.

The main interest of the study involved mapping basement-to-surface structure, basement topography, and locations of igneous intrusions, which appear to be linked to CO_2 reservoirs. It is hypothesized that CO_2 is sourced from the upper mantle and emplaced in high-porosity reservoirs through conduits that allow the migration of magmatic fluids to the surface (Gilfillan et al., 2008). These conduits are most likely planes of weakness, such as faults and fractures, at the basement level that have been reactivated over time. Identifying intrusions and conduits at depth provides a better understanding of CO_2 migration, pathways, and reservoirs.

In this study, we present the results of a CO_2 exploration strategy based on integration of public-domain gravity data with newly acquired ground magnetotelluric (MT) and airborne magnetic and electromagnetic (*Z*-axis tipper electromagnetic or ZTEM) data (Lo and Zhang, 2008; Lo et al., 2009), along with existing well and seismic data. The integration of these data sets is used to produce a series of 2D and 3D geophysical models that better define basin architecture over the entire region. We also combined these data in a quantitative approach using predictive analytics methodology to highlight areas of higher CO_2 potential.

The study area is located in southern Colorado, a region where seismic imaging is exceptionally limited due to the mountainous terrain and the presence of high-velocity volcanic rocks, which inhibit adequate resolution of the structural complexity at depth. Additionally, the scarce nature of regional public-domain data, along with the difficulty to obtain access and data acquisition permits from government agencies and land owners, makes this area challenging for conducting ground surveys. Procurement of airborne data, on the other hand, proved to be efficient in timing and in meeting survey requirements. The survey area covers 1106 mi^2 and is located on the northern edge of the Raton Basin, bound on the west by the Sangre de Cristo Mountains and on the east by the Wet Mountains and the Apishapa Arch (Figure 1). This basin is the southernmost Laramide foreland basin associated with the development of the ancestral Rocky Mountains. The western edge of the Raton Basin is composed of strata that are mostly vertical or overturned and generally fragmented by

[1]NEOS Inc., Walnut Creek, California, USA. E-mail: solvelasco@yahoo.com; lalumbaugh@gmail.com; manu@schnetzler.com.

Manuscript received by the Editor 1 December 2017; revised manuscript received 29 January 2018; published ahead of production 24 March 2018; published online 26 June 2018. This paper appears in *Interpretation*, Vol. 6, No. 3 (August 2018); p. SG59–SG78, 14 FIGS.
http://dx.doi.org/10.1190/INT-2017-0215.1.

west-dipping high-angle reverse faults and thrusts (Northrop et al., 1946; Merin et al., 1988). Strata along the western margin of the basin are also associated with Tertiary igneous intrusions, basalt flows, and dikes. The eastern side of the basin is only mildly deformed by folding and faulting.

During the Laramide Orogeny, in the late Cretaceous through the early Tertiary, the Raton Basin deepened dramatically, resulting in a stratigraphic sequence of more than 6096 m (20,000 ft) of lower Paleozoic through Tertiary sedimentary rocks in the deepest part of the basin (Popov et al., 2001; Sims et al., 2001). From late Oligocene to the present, the Sangre de Cristo Range was uplifted and the adjoining San Luis and Wet Mountain Valleys were down-dropped by Rio Grande rifting (Lindsey et al., 1983). Rifting accompanied and followed intrusion of stocks, sills, and dikes of felsic and mafic igneous rock.

In terms of the stratigraphy, the base of the sedimentary section consists of a thin carbonate succession (Devonian/Mississippian) that overlies the Precambrian basement. On top of this sequence are 1524–3048 m (5000–10,000 ft) of terrigenous Permian-Pennsylvanian strata, composed largely of sandstones and redbeds. Triassic redbeds (approximately 304 m [1000 ft] and up to 152.4 m [500 ft]) of terrigenous Jurassic sediments follow. The Cretaceous section includes 60.9 m (200 ft) of the basal sequence of clastic Purgatoire/Dakota Formation, followed by up to 609.6 m (2000 ft) of marine chalks, marls, and the organic-rich shales of the Benton and Niobrara Groups. This sequence is overlain by approximately 762 m (2500 ft) of the Pierre Shale. The marginal marine, partly deltaic Trinidad Sandstone overlies the Pierre Shale, which in turn is overlain by the coal-bearing Vermejo Formation and the Upper Cretaceous/Paleocene coal-bearing Raton Formation (Stevens et al., 1992). Tertiary sediments of the Poison Canyon Formation overlying these strata are highly variable and represent continental terrigenous sedimentation during the end of the Laramide orogeny. It is likely that approximately 3048 m (10,000 ft) of Tertiary sediments were originally deposited; however, erosion has removed much of the sediments, especially around the basin margins (Stevens et al., 1992).

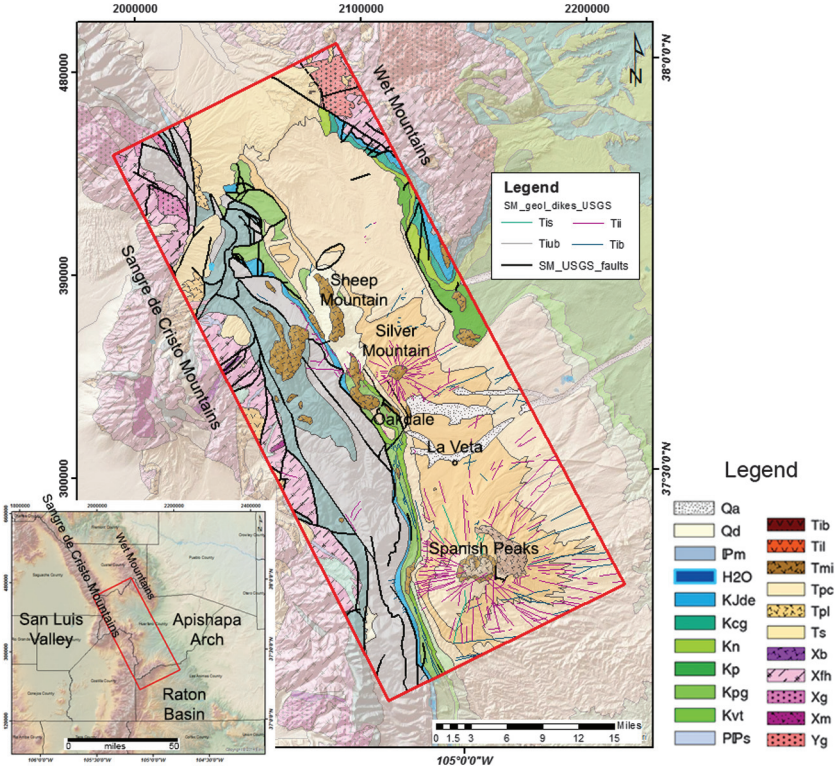

Figure 1. Geologic map of the study area showing major faults (SM_UGSGS_-faults) and Tertiary volcanic dikes (Tis: silicic intrusion, Tii: intermediate intrusion, Tib: basic intrusion, and Tiub: ultrabasic intrusion, from USGS, 2005). Geologic units include: Qa: Quaternary alluvium, Qd: Quaternary glacial drift, Tib: Tertiary basic intrusion, Til: Tertiary andesite, Tmi: Tertiary phaneritic plutonic intrusion, Tpc: Poisson Canyon Formation, Tpl: Tertiary andesite and tuff, Ts: Tertiary siltstones, KJde: Jurassic and Cretaceous Dakota and Entrada Sandstones, Kcg: Cretaceous shale, Kn: Cretaceous Niobrara Formation, Kp: Cretaceous Pierre Shale, Kpg: Cretaceous Purgatoire Formation, Kvt: Cretaceous Vermejo and Trinidad Formations, PPs: Permian-Pennsylvanian sandstones, Pm: Minturn Formation, Xb: Early Proterozoic biotitic gneiss, Xg: Early Proterozoic granites, Xm: Early Proterozoic gabbro, and Yg: Middle Proterozoic granites (from USGS, 2005). The NEOS survey area is shown in red polygon. Map of the location of the study area for reference (lower left).

Paleocene through Miocene time included the waning stages of the Laramide orogeny and intensive periods of igneous intrusion and volcanism (USGS, 2005). Widespread Tertiary extrusions are likely underlain by larger intrusions (e.g., Lipman, 1984). From 26.6 to 21.3 Ma, the voluminous volcanic eruptions and intrusions were sourced from the upper mantle and are represented by the west and east Spanish Peaks stocks (Johnson, 1991; Penn, 1994; Penn et al., 1994).

Most CO_2 deposits discovered to date have been the by-product of exploration efforts for hydrocarbons. Primary production of gas in the region has been CO_2 from two main fields, Sheep Mountain and Oakdale, located close to the northwest boundary of the Raton Basin (Figure 1). These CO_2 fields are similar to conventional natural gas fields, with the gas trapped in anticlinal structures. These are subthrust anticlines beneath the main thrust front aligned along a common northwest-trending trace and are Laramide in age (Eppink et al., 2014). The Sheep Mountain field produces CO_2 from the thin Dakota (60.9 m [200 ft]) and Entrada (30.4 m [100 ft]) Sandstones at a depth of approximately 1524 m (5000 ft), and sealed by the Pierre Shale and the Sheep Mountain

laccolith. The now declining Sheep Mountain field has produced 1.2 trillion cubic feet of CO_2 from 1983 to 2002. The Oakdale field produces CO_2 from the same thin sandstones, mentioned above, at 1828.8 m (6000 ft) depth, and one unconventional zone, which is a 91.4 m (300 ft) thick, shallow-dipping, felsite dike that has primary and secondary fracture porosity and permeability.

Methodology and results

Geophysical data acquisition

Critical to meeting the objectives of the project and identifying potential new CO_2 exploration areas for drilling, NEOS GeoSolutions, Inc. undertook a multimeasurement, geologic, and geophysical study over an area of southern Colorado, outlined in Figure 1. As part of this study, we analyzed public-domain gravity data along with newly acquired airborne magnetic and ZTEM data and ground MT data. These data sets were first analyzed individually and were later integrated with seismic and well data to build a geologic model of the area of interest.

Gravity data

The gravity data used for this project originated from the University of Texas, El Paso (UTEP), which has compiled ground gravity data in point data format for the entire United States. We downloaded these data for the specific project area, which are better in quality and detail than grid-based data from other sources. These data can be accessed through UTEP (2008).

We downloaded the UTEP free-air corrected data. The local UTM position information for these data was converted into the appropriate projection (Nad27-CoS-state plane-US feet), and the complete Bouguer gravity (CBG) correction was applied following standard processing procedures. The density used for the Bouguer slab and terrain correction was 2.67 g/cc, and the elevation information used for the terrain correction was the SRTM 30 m data set (SRTM, 2000). After the CBG data were calculated at each point, the data were interpolated and gridded to produce the map shown in Figure 2a. The station locations are marked by black dots. The gravity measurements are distributed mainly along roads and other areas of easy access for ground measurements. Therefore, there are large gaps where no data exist, as observed in Figure 2a.

Airborne geophysical data

For the airborne data acquisition, the survey area covers 1106 mi^2, which involved 1947 flight line miles at 999.7 m (3280 ft) line spacing, including the tie lines (Figure 2b). The region includes portions of the Sangre de Cristo Mountains as well as the Raton Basin, and there is more than 2133.6 m (7000 ft) of topographic variation within the survey area. Using a helicopter to collect the data allowed for a closer drape to topography than would have been possible by a standard fixed-wing aircraft. The typical mean terrain clearance of ZTEM and magnetometer acquisition systems is 50 m (164 ft) above the surface. However, due to the rugged terrain and rapid elevation changes, the safety of the aircraft and pilots took priority in the survey. This resulted in a terrain clearance of the acquisition systems between 48.7 and 182.8 m (160 and 600 ft).

The airborne magnetic data were collected concurrently with the airborne ZTEM data by Geotech in July and August of 2015. The helicopter-borne acquisition provided higher resolution magnetic data than was publicly available. During the same time period, ground

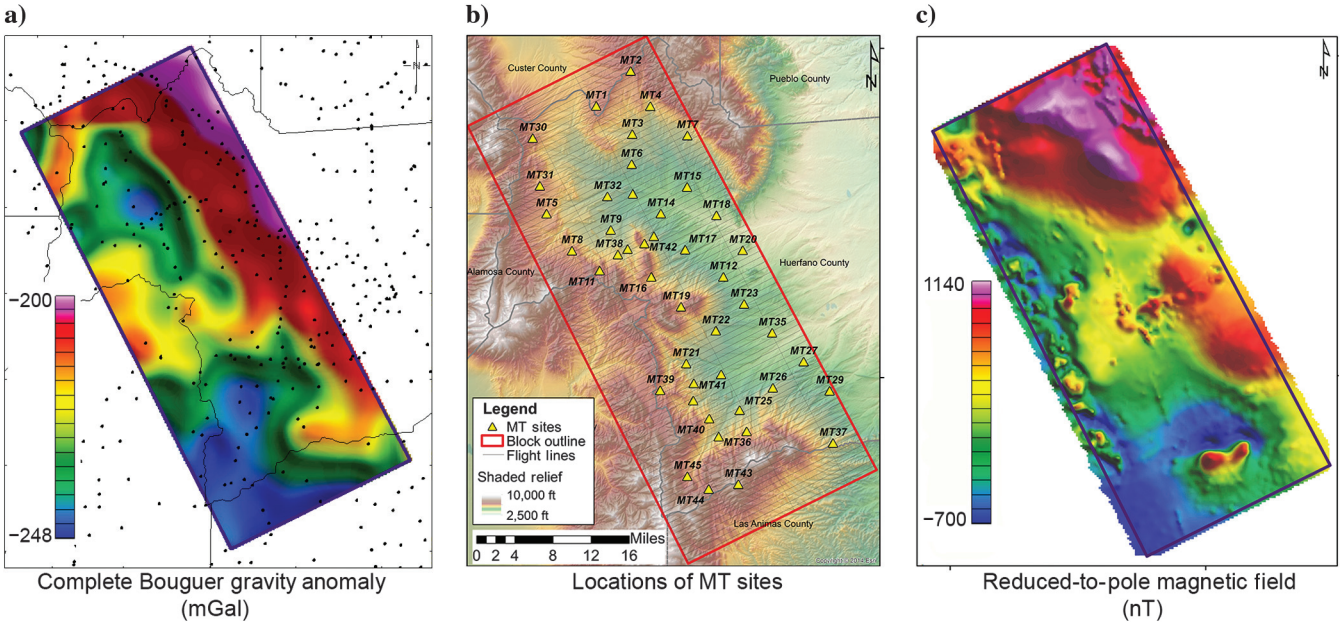

Figure 2. (a) The CBG with ground stations shown in black dots. (b) Map of the study area with airborne survey flight lines (solid black lines) and ground MT station locations (yellow circles). (c) RMI magnetic field data with survey lines for reference.

MT data were acquired from 44 ground sites (Figure 2b). It is important to note that the number of sites as well as their locations were constrained by permitting issues and access restrictions in the rugged terrain.

Airborne magnetic data

Due to the number of shallow igneous intrusions present in the study area, the airborne magnetic data contained prominent high-amplitude signals with high spatial-frequency content. This type of signal made line-by-line quality assurance and quality control (QAQC) and processing more challenging. However, the data are of very good quality and passed the high QAQC standards set forth at the beginning of the project as listed below:

- No data gaps.
- The magnetometer noise will not exceed 0.5 nT. The high-frequency noise envelope on magnetic data, as computed with a fourth difference filter, shall not exceed $+/-0.5$ nT over a distance of more than 2000 m.
- A base station magnetometer records data at 1 s intervals. Reflights will be flown at the seller's expense when the diurnal variation as recorded by the base magnetometer shows departures of 10 nT or more from a chord 5 min in length.
- The data had to show continuity of major anomalies from line to line.

As mentioned above, a magnetic base station within the survey area was used to record the diurnal variations of the magnetic field, which were used to correct for diurnal drift in the airborne measurements. To make the diurnal correction, a 50 s low-pass filter was applied to the base station data prior to application to the airborne data. This correction rectifies most of the acquisition-line imprint present in the data.

Due to the nature of the acquisition system using a helicopter, the magnetic data do not require a typical line-leveling procedure. Nevertheless, any line-to-line noise remaining after the diurnal correction has been applied was removed using a simple lag correction of three time samples (or 1.2 s). Finally, a manual decorrugation filter was applied using Geosoft Oasis Montaj software (Geosoft, 2015a) to remove any remaining line-to-line noise. Decorrugation filter tolerances were minimal and had little effect on the final output grid. We produced a total magnetic intensity and a residual magnetic intensity (RMI) grid. The RMI grid was created from the corrected full-amplitude data with the International Geomagnetic Reference Field (IGRF) removed (Figure 2c). To account for varying dates of survey acquisition, we used IGRF data corresponding to the survey midpoint date. This process removed the component of the earth's magnetic field related essentially to the earth's core from survey data. Next, we applied a transformation to convert the measurements to a data set that would be measured if the data had been collected at the magnetic pole, where the inclination of the earth's magnetic field is 90°. By applying this reduced-to-pole (RTP) transformation, magnetic signatures are positioned closer to the locations of their geologic sources on the magnetic maps, assuming the absence of remanent magnetization and self-demagnetization. In the survey area, the magnetic inclination is currently 64.5°, declination is 8.36°, and the total magnetic field intensity is 51,045.15 nT. The RTP data (Figure 3b) were then used to generate a set of derivative grids that were later used for interpretation.

Airborne electromagnetic data

Similarly, ZTEM data QAQC was performed on a flight-line by flight-line basis. The preliminary data consisted of in-phase and out-of-phase tipper values (measured in the inline and crossline directions) at six frequencies (30, 45, 90, 180, 360, and 720 Hz), along with a power-line monitoring channel (see Weidelt and Chave [2012] for a complete description of the tipper as a MT measurement). The first level of analysis involved determining that no data gaps existed along the flight lines for any of the channels, which was followed by a visual inspection of data quality. This was followed by additional QAQC procedures designed to evaluate the data via EM theoretical considerations. During the ZTEM survey, the contractual specifications were met for all flight lines. Figure 3c shows the 30 Hz inline, in-phase component of the tipper data. This represents the lowest frequency and, thus, the deepest sensing component of the acquired airborne tipper data set.

Ground magnetotelluric data

The ground MT data acquisition was completed by Zonge International from 27 July through 20 August 2015. Forty-five MT stations were planned; however, because livestock disturbed the equipment during acquisition, we were forced to drop one of the stations. Figure 3c shows the distribution of the 44 stations across the survey area superimposed on the inline ZTEM flight line map.

After assessing the data quality for each MT station, it was determined that most sites exhibited excellent quality, demonstrating continuity and coherence across most of the frequency spectrum for most stations. There is limited noise contamination due to cultural influences such as pipelines, power lines, and other anthropogenic sources of noise, especially for those sites that are closer to the town of La Veta (see Figure 1 for the location).

The increased noise appeared to be present both at the highest frequencies, ranging from 1 kHz (0.001 s) to 800 Hz (0.00125 s), as well as for frequencies less than 0.01 Hz (100 s). This influence is shown through increased error estimates and inconsistent curve shape and behavior, particularly when examining the phase curves (Alumbaugh et al., 2016). Due to this increased noise at the lowest and highest frequencies, these data

were eliminated from the curves and not included in the modeling. In terms of the frequency overlap between the two EM data sets, the airborne tipper data span six frequencies over the range of 30–720 Hz, and the MT data are processed to provide frequency data between 0.001 Hz and 1 kHz (Figure 4).

A non-1D geoelectric structure will cause separation of the apparent resistivity and phase curves as the period increases (or the frequency decreases) because with an increasing period, the MT signals become more sensitive to structures farther away from the site, as well as below it (Jones, 2012). The MT data predominantly depict 1D behavior at frequencies higher than 1 Hz, with the apparent resistivity and phase curves overlying one another. However, at approximately 1 Hz and below, the apparent resistivity and phase curves begin to split, indicating the onset of sensitivity to deeper regional geoelectric structure that is not 1D. Although most of the sites show this split occurring approximately 1 Hz, there are a few stations with sensitivity

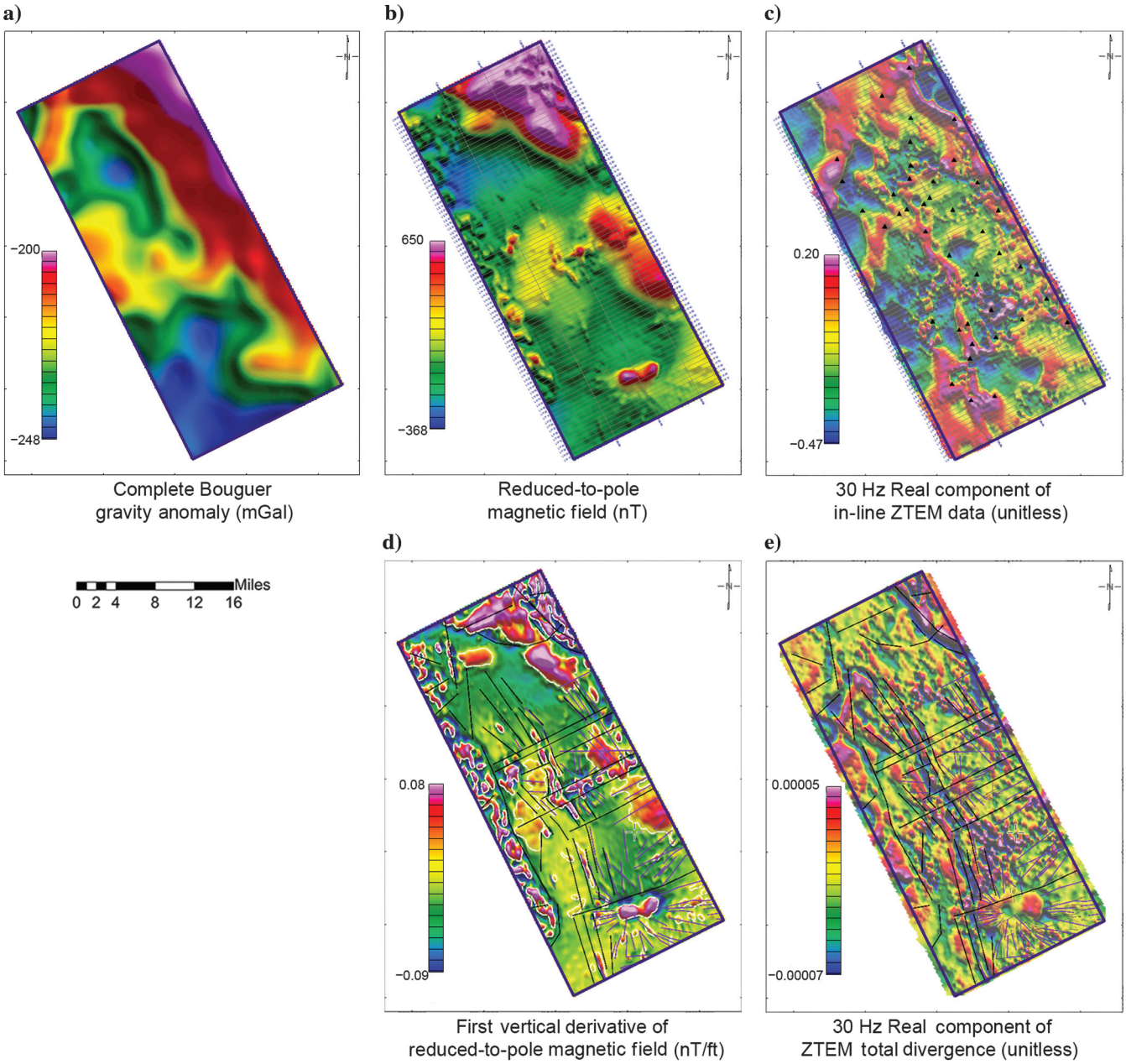

Figure 3. (a) The CBG with general interpretation (solid black lines represent northwest trending faults, dashed black lines represent possible northeast-trending faults). (b) RTP magnetic data with survey flight lines as gray solid lines. (c) Inline component of the airborne in-phase 30 Hz ZTEM data with survey flight lines as gray lines and ground MT sites represented by black triangles. (d) First vertical derivative (dz1) of the RTP data with interpretation of faults (black lines), volcanic dikes (violet lines), and magnetic bodies outlines (white polygons). (e) Total divergence of the in-phase 30 Hz airborne ZTEM data with superimposed structures and dikes interpretation derived from magnetic data for comparison.

to a 2D/3D structure as high as 10 Hz (0.1 s), signifying the increased geoelectric complexity at those locations (Alumbaugh et al., 2016).

Geophysical data interpretation

The Sheep Mountain and Oakdale CO_2 reservoirs of interest are associated with igneous intrusions and linked to faults that were likely used as pathways for CO_2 migration (Figure 1). Understanding the tectonic history of the region can help explain the location of these reservoirs and aid in finding additional concentrations of CO_2. With this as an objective, all geophysical data sets were first examined independently and later used together to create a consistent geologic model. To initiate the geophysical data analysis, gravity and magnetic data were interpreted individually using various derivatives and filters to produce gravity and magnetic structural interpretation maps (Figure 3a, 3b, and 3d).

Although the public domain gravity data points are sparse and yield a relatively low-resolution grid, the northwest to southeast trend associated with the major structural trend in the region is clearly reflected in the gravity map (Figure 3a). The interpretation of faults from the CBG grid correlates well with regionally mapped faults documented in the literature and with the interpretation of 2D seismic data. Thus, these gravity data were used for deep fault interpretation away from the location of the 2D seismic lines. In addition to the dominant northwest–southeast trend, the data also indicate a northeast–southwest trend expressed as a broad gravity high through the center of the survey region that separates two large gravity lows. The structural interpretation of this feature could be that it is a region of uplifted or elevated basement between two subbasins or a region of higher subsurface density related to the presence of buried mafic intrusions, given the widespread presence of intermediate to mafic volcanic rocks in this region.

The high spatial resolution provided by the newly acquired magnetic data allowed us to map more faults, and it was invaluable for locating igneous intrusions. We found the first vertical derivative (dz1) (Figure 3d) of the RTP data particularly useful when tracing these geologic features laterally, away from the areas where these features are better exposed. Once more, the main northwest–southeast trend observed on the gravity map is well-recognized, and a perpendicular northeast–southwest trend through the center of the study area is strongly suggested by a positive, partially linear magnetic anomaly; though it is narrower than the broad high observed in the gravity map. This positive trend is observed between two magnetic field lows in the original RTP data (Figure 3b) that could be partially correlated with the location of the gravity lows. Because the magnetic data are of higher resolution than the gravity data, the exposed intrusions and the surface volcanic features within this region are correlated to the higher elevated magnetic field and are very apparent in the magnetic image. This suggests that the highs in the gravity and magnetic fields along the previously described northeast–southwest geophysical trend are linked to mapped volcanic units and subsurface intrusions, rather than to an elevated basement surface.

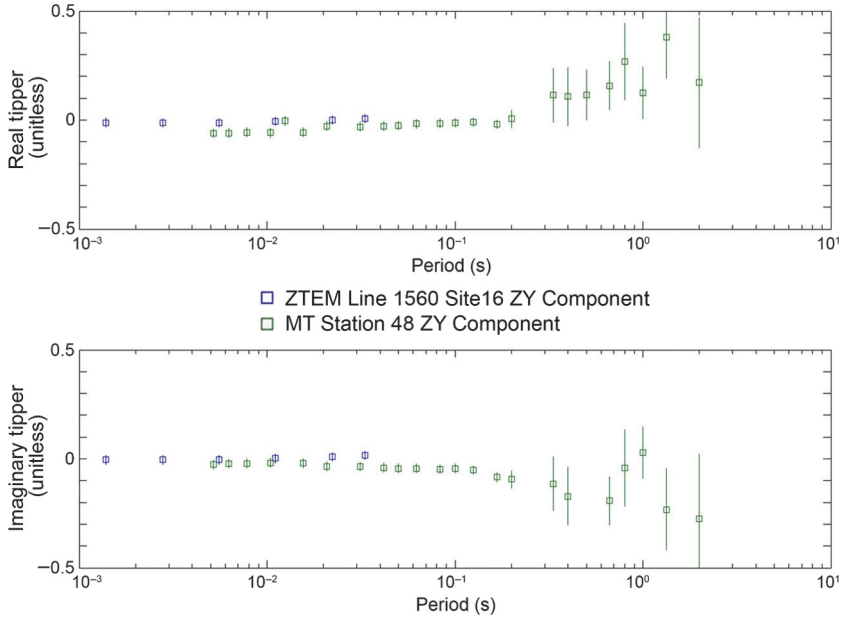

Figure 4. Plot showing the frequency overlap between the ground MT measurements and the airborne ZTEM tipper measurements. The green squares represent the component of the ground tipper measurements at MT station 48 rotated to the same direction as the ZTEM flight line, whereas the blue squares represent the inline component of the airborne ZTEM tipper data measured along a flight line located close to the MT station. The upper plot is the real or in-phase component, whereas the bottom plot shows the quadrature or out-of-phase component.

Initial interpretation of the airborne tipper data was carried out using maps of the total divergence (e.g., Figure 3e). Total divergence is calculated from the horizontal derivatives of the inline and crossline tipper transfer functions. It exhibits a minimum over a conductor and a maximum (peak) over a resistor (Lo and Zhang, 2008). Similarly to the magnetic and gravity data, the airborne ZTEM data also define the main northwest–southeast structural trend (Figure 3e). This image has the fault interpretation from the magnetic data overlain to show the excellent correlation between two completely separate data sets, corroborating the interpretation of the main structural trend (northwest–southeast) and locating major igneous intrusions, such as the Spanish Peaks and Silver Mountain (compare with Figure 1).

This preliminary interpretation derived from all geophysical data sets independently not only reveals the ma-

jor northwest–southeast structural trend, but it also suggest a perpendicular northeast–southwest trend, mainly observed in the magnetic and gravity data. This latter trend is likely related to ancient faults associated with Precambrian suture zones. Regional crustal studies position the survey area within a region of complicated, bivergent subduction events between two major Precambrian terranes, the Yavapai and Mazatzal provinces (Karlstrom and Humphreys, 1998). During the Precambrian, northeast–southwest convergence between these major provinces caused successive episodes of slab flattening and slab rollback, which led to crustal shortening and rifting, respectively. These complex tectonic episodes are thought to have formed faults in the cratonic platform crust, which were then reactivated by stress transmitted during Phanerozoic compressional orogeny in the mid-continent (Marshak et al., 2000). Sims et al. (2001) divide the basement in this region into blocks whose boundaries have northwest–southeast orientations consistent with Laramide structuring; however, they are interpreted as having variable movement through time due to the changing stress fields. These authors also recognize a northeast–southwest trend of which they define as shear zones. During the Pennsylvanian, the ancestral Rocky Mountains existed as intracratonic block uplifts formed by collision of the North American and South American-African plates (Kluth and Coney, 1981; Kluth, 1986; Burchfiel et al., 1992). Deformation of the central region of the continent during this time spread northwestward, and the Ancestral Rocky Mountains developed rapidly (Kluth and Coney, 1981). Inversion of basement-penetrating normal faults occurred during the late Paleozoic Ancestral Rockies event and/or during the Mesozoic-Cenozoic Laramide event. These tectonic features, divided into two sets on the basis of orientation (northeast and northwest), formed by inversion of Proterozoic extensional-fault systems (Cooper and Williams, 1989; Marshak et al., 2000). The geophysical data analyzed in this study reveal faulting that could be related to the Proterozoic accretionary model of North America (northeast–southwest), as well as northwest–southeast faulting that has been rejuvenated during the Laramide Orogeny.

As noted above, the study area is dominated by igneous features such as dikes, sills, hypabyssal plugs, and laccoliths. The area has a well-developed and exposed dike system associated with major stocks, such as the Spanish Peaks and Silver Mountain (Figure 1). The various orientations and compositions of these diverse features signify a complicated history of eruptive events.

According to the literature (e.g., Christiansen and Lipman, 1972; Lipman et al., 1972; Mutschler et al., 1988), there were three major magmatic episodes during the Laramide orogeny, during which regional stresses transitioned from compression to extension. The first episode was caused by regional deformation and associated compressional stresses. The second episode was related to the initiation of regional extension. The third episode was associated with the northward propagation of the Rio Grande Rift, which is also believed to have caused the development of the Spanish Peaks (Penn and Lindsey, 2009).

In hydrocarbon exploration, identifying igneous intrusions is an important factor in regard to drilling hazards. However, in CO_2 exploration, the presence of intrusions is also closely related to CO_2 production. As mentioned earlier, the study of noble gases found in CO_2 reservoirs performed by Gilfillan et al. (2008) revealed that most of the CO_2 present in the Sheep Mountain region was sourced from the upper mantle. Therefore, identifying intrusions and conduits at depth may provide a better understanding of CO_2 accumulation.

To emphasize and isolate the position of igneous bodies and intrusions, and the position and orientation of igneous dikes, we analyzed the first vertical derivative of the magnetic RTP data (Figure 3d). Based on field observations, published studies, and our interpretation of the newly acquired magnetic data and their derivatives, four dike orientations are recognized: radial, northwest–southeast, northeast–southwest, and east–west (Figure 3d). The radial dikes appear to be associated with the same magmatic pulse as the volcanic plug in their center (Johnson, 1968). The northwest–southeast-trending dikes are parallel to the major structural trend throughout the area. The northeast–southwest-trending dikes are perpendicular to this major structural trend and parallel to the interpreted suture zones at basement depths. The northeast–southwest dikes are also the longest and can extend up to 17 mi at the surface. East–west-trending dikes are less common; however, they are observed around the Spanish Peaks area. According to Johnson (1968), these dikes could be different in age from that of the radial dikes system, perhaps related, but separate episodes of magmatism.

Based on the interpretation of filtered magnetic data, the intrusions mapped at the surface, appear to continue downward in most cases, although the depth of these is unresolvable using the magnetic data alone due to the nonuniqueness of the method. The magnetic bodies interpreted at depth from the first vertical derivative of the RTP data and not observed at the surface are likely sources of the isolated shallow igneous bodies and dikes observed, in particular, on the eastern part of the study area. The Precambrian basement rocks exposed in the Sangre de Cristo Mountains and the Wet Mountains are intruded by younger, tertiary igneous rocks (Clark, 1966). The magnetic character of the basement that forms these two mountain ranges is different from that of the rest of the igneous bodies found in the region. The Precambrian basement has lower magnetic susceptibilities than the surrounding, younger magnetic bodies observed and measured at the surface. These observations indicate an episodic history of intrusions, which can have implications for CO_2 emplacement.

2D modeling

To determine a starting point for modeling of the various geophysical data sets, and to provide a basis for understanding the geologic structure and relationship between the sedimentary basin and the Precambrian basement, several 2D geologic cross sections were constructed based on the combination of information and constraints provided by surface outcrops, seismic and well data, and constraints provided by the magnetic and gravity data. These 2D sections were oriented perpendicular to the northwest–southeast-trending regional structure to better model the geology, and they were based on key well locations and available public domain data. In areas where published cross sections along seismic lines and well-data interpretation were available, such information was also used to better constrain the Phanerozoic stratigraphy of the Raton Basin.

The profiles were created using Geosoft GM-SYS Profile modeling v. 8.4 (Geosoft, 2015b) gravity and magnetic modeling software, which is based primarily on the methods of Talwani et al. (1959) and Talwani and Heirtzler (1964). We used this software to build geologic models with the public-domain ground gravity data and the airborne magnetic data acquired in the study area. Then, we constrained these models with surface geology, published cross sections, well data, density and magnetic susceptibility measurements of outcrop samples, seismic interpretations, and newly acquired EM data.

The 2D profiles represent a generalized interpretation of the geology of the area constructed to fit the magnetic and gravity data. For the gravity data, we used the CBG anomaly data shown in Figure 2a. For the magnetic data, we used the RMI data shown in Figure 2c and field parameters listed in the section above.

Each geologic unit was assigned a density and susceptibility value, which were determined from measurement of field samples. If field samples were inaccessible, density values were determined from geophysical references and susceptibility values estimated for specific rock types and a susceptibility table published by Telford et al. (1990). After applying density and susceptibility attributes to each unit in the model, we completed several inversion iterations to improve the match between observed and calculated gravity and magnetic anomalies.

Two examples of the derived 2D models are shown in Figures 5a and 6a. These figures show the most representative stratigraphic layers and geologic units of interest. The basement is represented by the pink color with a fill pattern, Paleozoic sediments in gray, Mesozoic in blue and green, and Tertiary and Quaternary in beige. Igneous intrusions are shown in gray with a fill pattern. The profiles include additional units that were probably not needed to match the potential field data, but were incorporated to produce geologic models that better indicate the structural interpretation. For instance, the Quaternary and Tertiary layers do not necessarily cause a change in the density or susceptibility models; however, they were divided into several units to highlight the complex structures (e.g., folds and fault offsets).

The sedimentary basin rests on the Precambrian basement. This basement interval was divided into separate blocks within the model, as noted by the vertical separations within the unit, to generally represent the lithologic heterogeneity of the Precambrian basement. We therefore modeled several different Precambrian blocks using field observations and measurements of magnetic susceptibility of basement outcrop of several different lithologies. The position of the top of the Precambrian basement was initially calculated by interpolating well data located outside of the study because of the lack of well penetration within the study area. The top of the basement represents the base of the Paleozoic within the sedimentary basin, and the contact between the basement and the sediments above is associated with the high magnetic susceptibility contrasts in the entire area, represented by long-wavelength high-amplitude responses. Similarly, the gravity data suggest that the highest density contrasts are across this major boundary between the sedimentary basin and the basement. The geometry and thickness of the sedimentary basin are constrained partly by borehole formation tops and were modeled initially to fit the gravity data. Short-wavelength responses are also observed in the magnetic data, and these anomalies are interpreted to represent shallow intrusions of Tertiary age, some of which are also exposed at the surface.

The 2D resistivity images were produced for each survey line inverted separately via a joint inversion of the airborne ZTEM and MT data using the algorithm outlined in Key (2012) and the workflow outlined in Alumbaugh et al. (2016). Because the data clearly exhibit 3D attributes, the use of the 2D code required additional processing and editing prior to inversion. In this regard, the ZTEM data did not need any rotation applied as the flight-line direction was chosen to be perpendicular to the regional geologic strike. However, to satisfy the 2D approximation, we only used the data corresponding to a tipper aligned with the flight-line directions. The other processing step applied to the ZTEM data was to manually eliminate those measurements that showed signs of powerline contamination. One last note to mention is that the ZTEM data were decimated from approximately a 6 m (20 ft) station spacing, as delivered by the vendor, to a 499.8 m (1640 ft) station spacing. This final step was done to not overload the available computer power. Therefore, the lateral resolution is 499.8 m (1640 ft) in the inline direction and 999.7 m (3280 ft) in the crossline direction. Given that the primary goal of the ZTEM survey was to supplement the sparse MT data to image the larger scale structure of the basin rather than image the near surface, decimating the data to this coarser scale prior to inversion had no detrimental effects on the analysis. Furthermore, this decimation provides similar resolution in the inline and crossline directions.

The first preinversion processing step for the MT data was to rotate the data to the same direction as the ZTEM flight lines. Next, data showing large 3D effects were deleted before the inversion process. This was accomplished through analysis of the various parameters that highlight the degree of 3D structure present in the data, as thoroughly described by Jones (2012), including the phase tensors shown in Figure 7. If any of these parameters suggested the presence of significant 3D structure, those particular data were not used in the 2D inversion. Additionally, the main diagonal of the impedance tensor could not be used because these parameters are only nonzero in the presence of 3D geology. This resulted in less than half of the processed MT data being used in the 2D inversion.

All 82 lines of the ZTEM data collected were mathematically inverted using the code from Key (2012). To incorporate the MT data, stations within 2 km distance of a given flight line were included. Although this implies that most of lines have at least one ground station associated with them, analysis of Figure 2b indicates there are many lines that have no associated MT data for inversion. The ZTEM data along the flight lines suffer from limited depth sensitivity and resistivity resolution, which yield quite different results for two adjacent lines, thus resulting in a geologically unreasonable interpretation. To circumvent this problem, we developed a "line-to-line" model constrained inversion approach, which is similar in nature to the "laterally constrained" inversion technique of Auken and Christiansen (2004). This method includes a "closest model"

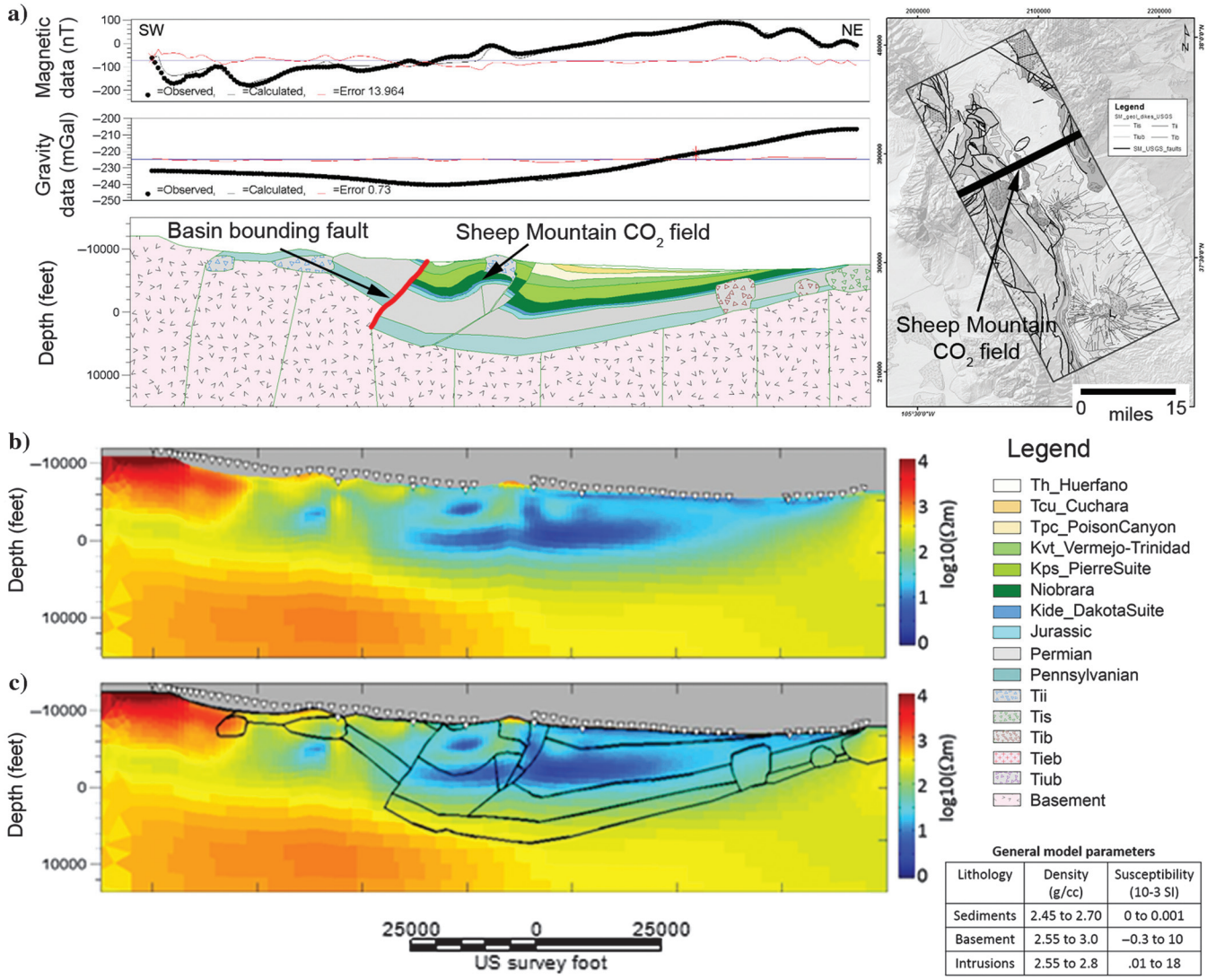

General model parameters

Lithology	Density (g/cc)	Susceptibility (10-3 SI)
Sediments	2.45 to 2.70	0 to 0.001
Basement	2.55 to 3.0	–0.3 to 10
Intrusions	2.55 to 2.8	.01 to 18

Figure 5. (a) Example of a 2D profile over the Sheep Mountain CO_2 field. Black circles in the magnetic and gravity panels above the section represent the input magnetic and gravity data, respectively. Black lines in the top two panels represent the values calculated from the models; the red line represents the difference or error between the measured data and calculated results. The top right corner shows the map with the profile location. Model parameters are immediately below. (b) Resistivity image, product of the joint inversion of the airborne EM and ground MT data. (c) The same resistivity image from above with the interpretation derived from the potential field section at the top of the figure.

formulation in the cost function to ensure that each line is as close to adjacent lines in terms of resistivity structure as the data will allow, thus providing coherency in the images perpendicular to the direction of the flight lines.

Figures 5b and 6b provide examples of this imaging procedure, corresponding to the same profiles as the potential field data and interpretation shown in Figures 5a and 6a. Analysis of the inversion results indicates a general increase of resistivity with depth within the geologic section, showing the lowest resistivity values within the Mesozoic sedimentary package. The latter is possibly related to higher porosity rocks and/or the presence of thick low-resistivity shale units. The basement is associated with relatively high-resistivity values, as are most of the outcropping and interpreted igneous intrusions. Specifically in Figure 5, the intrusion at the surface in the center of the section is indicated in the resistivity model as having higher resistivity than the surrounding sedimentary rocks. The basin is clearly outlined in the EM images, with a western boundary defined by a change in resistivity and represented in the potential field constrained geologic models as a major basin bounding fault, which is also observed at the surface. These two sets of independent models show similar characteristics and indicate geologic features that are in general agreement with one another (Figures 5c and 6c).

3D modeling

As part of the basin architecture study, we also generated 3D models with the potential field data. We used Geosoft's VOXI Earth Modeling software (Geosoft,

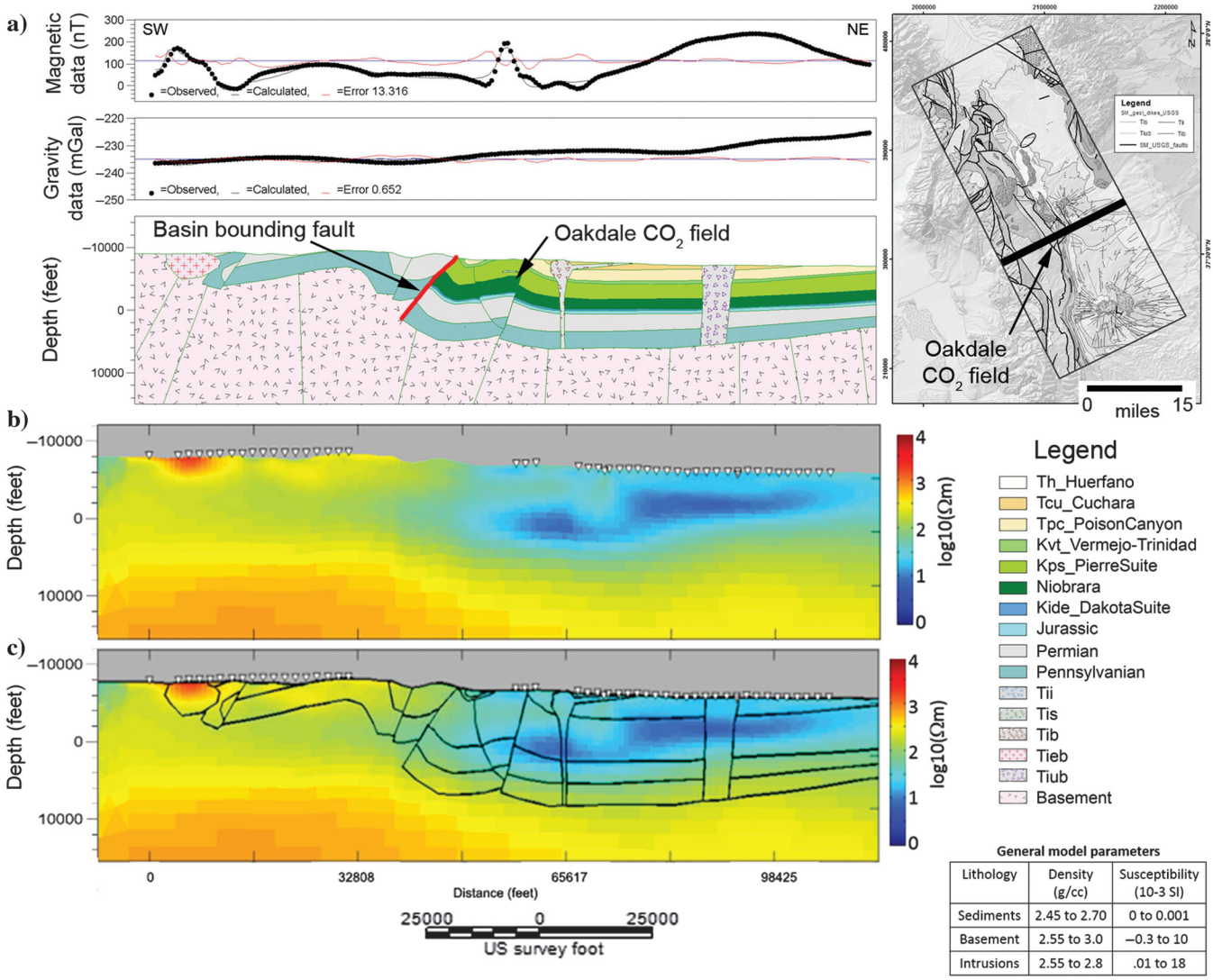

General model parameters

Lithology	Density (g/cc)	Susceptibility (10-3 SI)
Sediments	2.45 to 2.70	0 to 0.001
Basement	2.55 to 3.0	–0.3 to 10
Intrusions	2.55 to 2.8	.01 to 18

Figure 6. (a) Example of a 2D profile over the Oakdale CO_2 field. Black circles in the magnetic and gravity panels above the section represent the input magnetic and gravity data, respectively. Black lines in the top two panels represent the values calculated from the models; the red line represents the difference or error between the measured data and calculated results. The top right corner shows the map with the profile location. Model parameters are immediately below. (b) Resistivity image, product of the joint inversion of the airborne EM and ground MT data. (c) The same resistivity image from above with the interpretation derived from the potential field section at the top of the figure.

2015c) and service to produce 3D inversion volumes of the gravity and magnetic data. The airborne magnetic data were used to generate a susceptibility model, and public-domain ground gravity data were used to generate a density model. Due to the nonunique nature of the inversion of magnetic data to recover spatial distribution of the magnetic susceptibility, we added constraints to incorporate a priori geologic knowledge into the computation. A similar approach was used with the inversion of the gravity data.

Gravity data

The gravity data used in the 3D density modeling was the same Bouguer anomaly (CBG) grid shown in Fig-

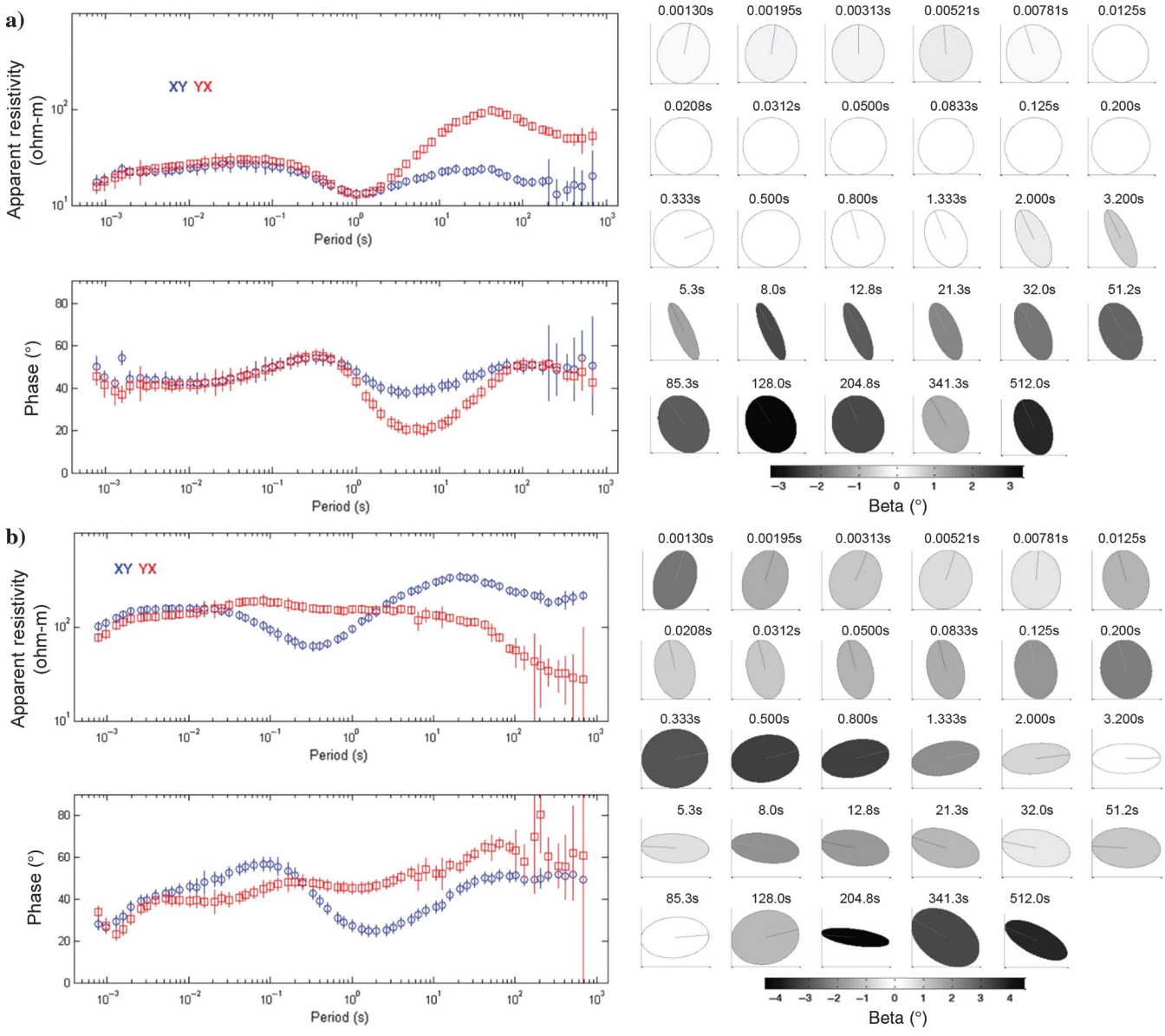

Figure 7. The MT data for (a) Station 29 in the southeast section of the survey area, and (b) Station 48 in the southwest section. The left side of each plot shows the apparent resistivity (top) and impedance phase (bottom) curves for each station, whereas the right side of each plot shows the phase tensor ellipses ranging from high frequency at the top to low frequency at the bottom. Frequencies where the XY and YX curves in the left plots lie on top of each other and the phase-tensor ellipses are circular with a beta angle near zero indicate that the region of the earth that the data are sensitive to is 1D. For frequencies where the XY and YX curves are separated, the phase-tensor ellipses are elliptical with the major axis generally aligned northwest–southeast, and the beta angle is approximately 2° or less, the data are generally indicating sensitivity to 2D structure aligned with the main structural axis of the area. For those frequencies in which the XY and YX curves are separated, the phase-tensor ellipses are elongated and not aligned with the main structural axis of the region, and the beta angle exceeds 2°, the data are sensitive to the 3D structure and these data were not included in the 2D inversions. For these two MT soundings, Station 29 does not show much 3D structure except at very long periods (low frequencies), whereas Station 48 is indicating the presence of strong 3D effects at periods greater than 0.33 s. See Figure 2b for station location.

ure 2a. Due to the sparseness of the data, the forward modeled gravity response and misfit were compared with values measured at the original gravity stations during the inversion process.

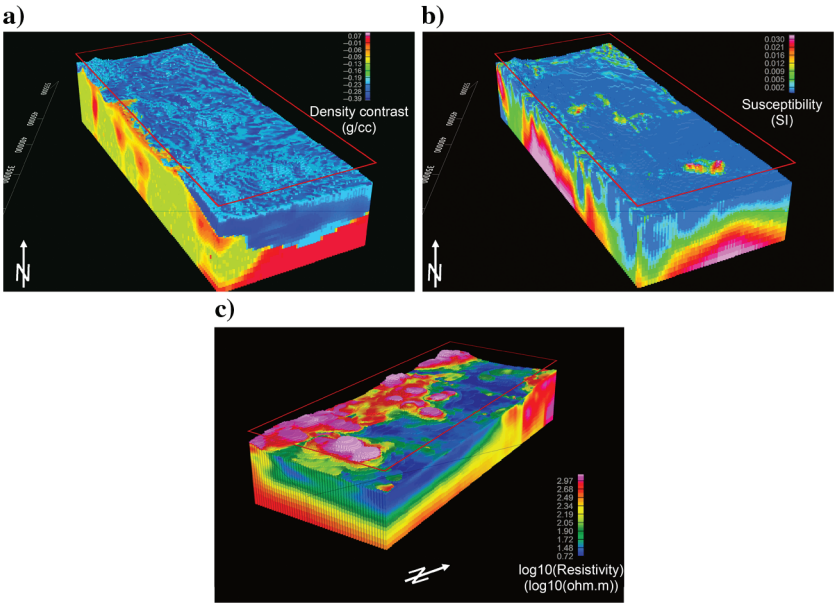

Figure 8. (a) The 3D density volume resulting from the constrained inversion of the gravity data. (b) 3D magnetic susceptibility volume resulting from the inversion of the RMI data. (c) 3D resistivity volume resulting from the merging of 2D joint inversions of the airborne ZTEM and MT data.

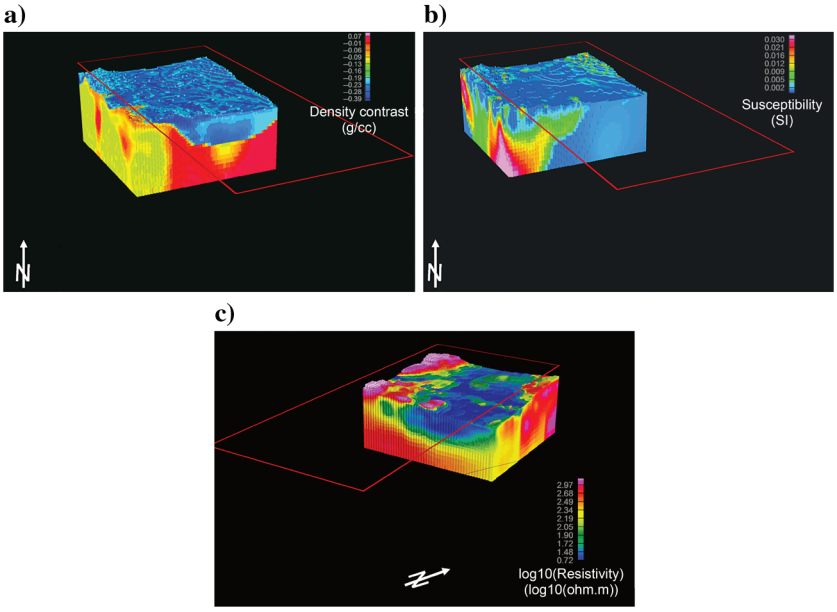

Figure 9. (a) Vertical slice of the 3D density volume. Note the high density contrast between the sedimentary basin (blues) and basement (reds), and the change in density within the basement on the western portion of the model. (b) 3D magnetic susceptibility volume resulting from the inversion of the RMI data. Note the higher magnetic susceptibilities related to igneous intrusions. (c) 3D resistivity volume resulting from the merging of 2D joint inversions of the airborne ZTEM and MT data. Note the high resistivity contrast between basin (blues) and basement (reds) and the isolated high-resistivity features representing igneous intrusions.

The inversion of gravity data to recover 3D spatial distribution of density is nonunique. Additionally, the sparse nature of the gravity data used for the inversion provides limited information on how density is varying with depth, and it only helped to resolve the larger scale basin and tectonic features. Thus, to make better use of the gravity data, we applied a constrained inversion that incorporated geologic, geophysical, and petrophysical (density logs) data as constraints to determine depth to basement across the area. This was accomplished using a nonuniform starting model that included upper and lower bounding constraints to help ensure consistency between the known geology and resulting distribution of density contrasts. The sedimentary and basement upper/lower density values were derived from our field campaign, published values from literature, and a priori knowledge. The results of the constrained density inversion are shown in Figure 8a. Figures 9a and 10a show the model slices that display the variability with depth.

Consistent with our field campaign, the density volume shows a less dense basement to the west. At first glance, the density model emphasizes our interpreted shape of the basin. This is due to the constraints we added to the inversion process, and it suggests that our interpretation of the basement provides a reasonable explanation of the gravity data. There is also a strong density contrast, against a reference density of 2.67 g/cc, observed in the basement on the western side of the area, in contrast to the more uniform density on the east side. This feature coincides with the location of the main northwest–southeast-trending thrust fault observed at the surface, suggesting the continuation of the prevailing regional northwest–southeast trend deep within the basement (Figures 8a and 9a). A high-density contrast is also observed in the northeastern portion of the survey area, highlighting the boundary between the basement rocks of the Wet Mountains and the basin (Figure 10a).

Magnetic data

Following a workflow similar to the one described for the gravity data, we used the gridded RMI data (Figure 2c) to generate a susceptibility model using the VOXI inversion code. Due to the

nonunique nature of the inversion of magnetic data to recover the spatial distribution of susceptibility, we added constraints to incorporate a priori geologic knowledge into the computation. For example, the susceptibilities of all rocks within the survey area are expected to be greater than or equal to zero. As such, we incorporated a lower bound constraint set to a constant of zero to ensure positivity. Similarly, we added an upper bound constraint designed as a simple two-layer model (above/below the top of basement). We assigned an upper susceptibility bound value of 0.1 SI units within the basement and 10 SI for the region above the basement. The presence of high magnetic susceptibility intrusions that outcrop at various locations in the basin, and which yielded high values of measured magnetic susceptibility using a hand-held meter in the field campaign, necessitated the use of high upper bounds.

A nonuniform starting model was used to initialize the inversion. The use of a nonuniform starting model is an implicit constraint because it will affect the final model reached by the inversion. In addition, a good starting model can significantly speed up the computation. The starting model contains susceptibility values of 0.05 SI in the basement, 0.1 SI in the sedimentary column where Tertiary volcanic rock exists, and 0 SI elsewhere in the sedimentary column.

A gradient reference and weighting constraints were used together to describe confidence in the location of the basement-sedimentary physical discontinuity, and we used the same location for this interface as used in the density starting model. The vertical gradient weighting featured values of 0.0001 SI along the top of the basement structure and 1 SI elsewhere. North–south and east–west gradient weighting constraints were included as constant values of 0.1 SI, which resulted in a 10 times smoothing factor vertically. This was enforced as intrusive bodies (e.g., dikes) are expected to feature a significant depth extent as opposed to lateral extent; thus, these constraints were designed to optimize the vertical continuity of dikes and other igneous bodies.

Figure 8b shows the inverted result as a 3D volume, whereas Figure 9b shows the model sliced in half to observe the variability in depth, and Figure 10b shows a depth slice at 457.2 m (1500 ft) above sea level. The susceptibility modeling result is consistent with known surface geology and sheds light on the shape and location of intrusive bodies in the shallower parts of the model. Due to the nonuniqueness of potential field inversion, the shape and depth of deeper magnetic bodies are possible, but not exclusive. Also note that the susceptibility model (Figure 10b) does not show the depth to basement and basin structure with the same coherency as the density model (Figure 10a). This is likely due to the presence of high-susceptibility magnetic intrusions observed at the surface masking effects of deeper structure, coupled with the possibility of large susceptibility contrasts within the basement itself.

Resistivity volume

The last processing step in the EM analysis was combining the 82 2D images of the airborne ZTEM and MT data into a 3D resistivity volume. This was achieved by first projecting each 2D resistivity section into its true 3D position, and then using a geostatistical 3D-gridding algorithm to interpolate between the lines onto a regular 3D grid shown in Figure 8c. The 3D resistivity model offers the best image highlighting basin features and the best estimate of basement depth, in comparison with the magnetic and gravity data. This model provides valuable information about basin geometry, including the lateral termination of Mesozoic younger clastic rocks against thrust faults bounding the western side of the Raton Basin. In addition, the 3D resistivity volume indicates a fairly consistent basement depth from northwest to southeast along the axis of the basin, providing further evidence that the northeast–southwest-striking region of elevated gravity and magnetic fields across the center of the survey region in Figure 2 is most likely related to subsurface intrusions rather than an elevated basement. The sedimentary basin boundary is well-defined by the abrupt change from a zone of low resistivity, highlighted in blue and associated with the Mesozoic package, to bordering zones of high resistivity associated with Proterozoic and Paleozoic formations, particularly along the western side of the basin (Figure 7c). The western basin bounding fault is clearly highlighted by a resistivity contrast that correlates well with the main structural northwest–southeast trend. This EM model best reflects the 3D nature of this structurally complex region.

The resistivity images from the EM inversion (Figures 5b and 6b) also suggest a less resistive zone beneath the resistive outcropping basement along the

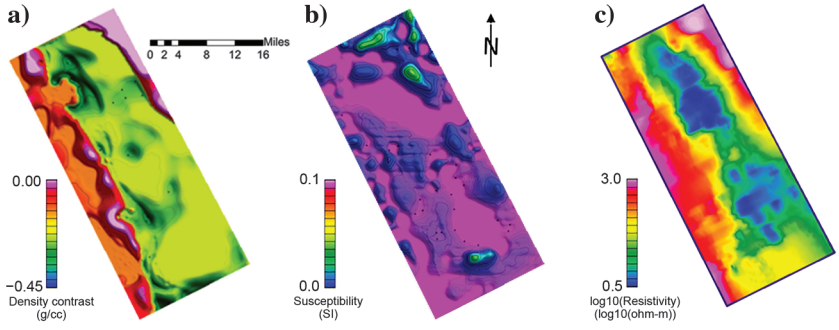

Figure 10. (a) Depth slice of the 3D density volume at 457.2 m (1500 ft) above sea level. (b) Depth slice of the 3D magnetic susceptibility volume resulting from the inversion of the RMI data at 457.2 m (1500 ft) above sea level. Note the higher magnetic susceptibilities related to igneous intrusions. (c) Depth slice of the 3D resistivity volume resulting from the merging of 2D joint inversions of the airborne ZTEM and ground MT data at 457.2 m (1500 ft) above sea level.

westernmost east-verging thrust fault that bounds the Sangre de Cristo Mountains. Our original hypothesis for the thrust faulting along the western edge of the basin, which is proposed by (Clark, 1966), is that of a high-angle thrust system with the Sangre de Cristo Mountains composed of older basement rock overlying younger basement rock. However, the low resistivity in the inversion results beneath these mountains suggests the possibility of a low-angle fault that would place the Precambrian basement over a sedimentary package. This interpretation is in agreement with previous work done by Ruleman and Machette (2007), and it would also explain the low-basement densities recovered to the west of the major fault thrust, via samples collected from surface outcrop, as indicated in the density model and shown in Figures 5a and 6a.

Because the presence of a sedimentary sequence beneath the Sangre De Cristo Mountains could have an impact on hydrocarbon and CO_2 exploration in the region, 2D EM forward modeling and inversion tests have been conducted using the resistivity image in Figure 5b as a test model. Because the inversion of EM data is well-known to be nonunique — that is, multiple resistivity models can produce the same data — the goal of these numerical tests was to try to determine if the presence of this low-resistivity zone is strongly supported by the data or if it is possibly an artifact of the ZTEM and MT data acquisition footprint coupled with the 2D inversion process. The first set of tests consisted of forward EM modeling using the resistivity distribution across the whole line as shown in Figure 5b. This resistivity model was used to produce a synthetic data set at the actual airborne ZTEM and ground MT acquisition locations using the 2D forward modeling code of Key and Weiss (2006). This is considered our "baseline" synthetic data set consisting of numerically calculated tipper and MT values that would be measured over a 2D earth that includes the low-resistivity zone beneath the mountains. Then, we made everything beneath the crest of the Sangre de Cristo Mountains a uniform high resistivity in our 2D model and ran the forward code again to generate a second synthetic data set. This second set of synthetic tipper and MT calculations is equivalent to what would be measured over a 2D earth with uniform high resistivity beneath the mountains. Calculating the difference between these two synthetic data sets indicates that a low-resistivity zone produces a 2%–7% difference in the airborne tipper data, which is well above the measurement noise level of the survey of 0.5%. Additionally, when these two synthetic data sets are inverted using the same methodology as used for the measured field data, the low-resistivity zone beneath the mountains only appears in the resulting image when it is explicitly contained in the model that generated the synthetic data.

A second possible mechanism for generating an artifact in the 2D images may be linked to the location of this low-resistivity zone at the western end of the ZTEM and MT lines. It is well-known that the MT methods are sensitive to distortions caused by lateral resistivity changes that can be located far away from the measurement location (for an explanation, see Jones, 2012). MT and other EM studies within the San Luis Valley, immediately west of the Sangre de Cristo Mountains, have shown that the valley contains a thick sequence of very low-resistivity sedimentary fill (Williams and Rodriquez, 2007; Ball et al., 2015). Therefore, to test whether the MT fields generated by this thick conductive sequence to the west of our field area might be "contaminating" our data, a second set of modeling and inversion tests was conducted extending the modeling domain further westward and including the full topography of the Sangre de Cristo Mountains, as well as a low-resistivity San Luis Valley. This test produced the same results as the first one, thus providing further confidence that this low-resistivity zone observed in the EM inversions is real. The results of these 2D MT modeling and inversion tests, coupled with the low densities that were recovered on the western side of the model from the 3D gravity inversion as shown in Figures 8a and 9a, give credence to the hypothesis that the main thrust fault on the western side of the basin is of a low angle and has emplaced basement material on top of the sediments. To verify which of the two possible thrust scenarios is more probable would require additional gravity data to be collected and modeled and a full 3D inversion to be run on the ZTEM and MT data.

Multimeasurement interpretation methods

Qualitative methods

We combined all available data sets with the ultimate objective of reducing the uncertainty of our interpretation for the study area. New interpreted dikes and faults not visible at the surface were added to this integrated model. The main northwest–southeast structural trend is evident, but the model suggests a northeast–southwest trend not clearly visible at the surface. The model also provides the location of intrusions at depth that, in some cases, appear to have a close relationship with CO_2 production. Figure 11 shows an interpretation map with published structures and dikes.

After we analyzed the data sets described above, we created an integrated 3D geologic model to ensure consistency with the seismic and well data, and to study the relationship between modeled densities, magnetic susceptibilities, resistivity, basement structure, and interpreted faults and intrusions (Figure 12). This multimethodology integration allows us to combine all relevant interpretation results in a single consistent 3D model. This 3D representation, in conjunction with geologic knowledge of the area, helped to identify additional potential CO_2 exploration targets.

Within this model, based on all data sets combined, we highlight the portions that are more useful in identifying potential areas associated with CO_2 production. Figure 12 shows low-resistivity isosurfaces equal to 10 ohm-m and high magnetic susceptibility bodies,

interpreted to be igneous intrusions. The figure also shows interpreted faults and dikes and the location of drilled wells. This type of 3D integration of results based on several methodologies helps to identify areas of interest.

Regions of higher CO_2 production are suggested to occur near magnetic bodies and dikes, and low-resistivity zones. These low-resistivity zones in the 3D volume are not directly related to the CO_2 reservoirs because the reservoirs are too thin to be detected from the surface, and are shown, through resistivity well logs, to be higher resistivity zones rather than lower. However, the low-resistivity zones are indicative of a thicker Cretaceous/Jurassic sequence that hosts the reservoirs. The analysis of resistivity well logs suggests that the lowest resistivities are produced by clay-rich Pierre shales located above the CO_2 reservoirs. These low-resistivity shales are thick, and due to the presence of clays, they have very low hydraulic permeability. Therefore, the aforementioned low-resistivity zones are likely indicating regions containing both reservoirs that are too thin and deep to directly detect, and a thick sequence of low-permeability shales that serve as excellent cap rocks to trap the CO_2 within the reservoirs.

Quantitative methods

Predictive analytics is the application of machine learning algorithms that explore complex relationships among multiple data sets and, for our use, predict the presence of economic resources (e.g., oil, gas, and CO_2) at unsampled locations. Several approaches within the general framework of machine learning can be applied to spatial data (depending on the problem, type, and amount of data), all designed to predict some specific variable away from known locations.

To estimate the CO_2 production potential of the region, we built a similarity grid from a set of 2D input grids (predictor variables) and a series of training locations. The assumption is that the input data grids are sensitive to various geologic attributes and, in particular, geologic features relevant to CO_2 production and storage, even if this relationship is not known precisely. At each location (x, y) of the 2D input grid, we calculate the normalized Euclidean distance between the vector of predictor values at (x, y) and the vector of predictor values at each training location. The distances calculated for each training location are combined to build a distance between the location (x, y) and the set of training locations. This procedure is repeated for each point of the input 2D grid, resulting in a complete distance grid. This grid is inverted to a similarity grid representing areas having similar characteristics to the areas of training locations — high values indicate areas similar to the training locations (for the input grids selected), whereas low values indicate areas dissimilar to the training locations.

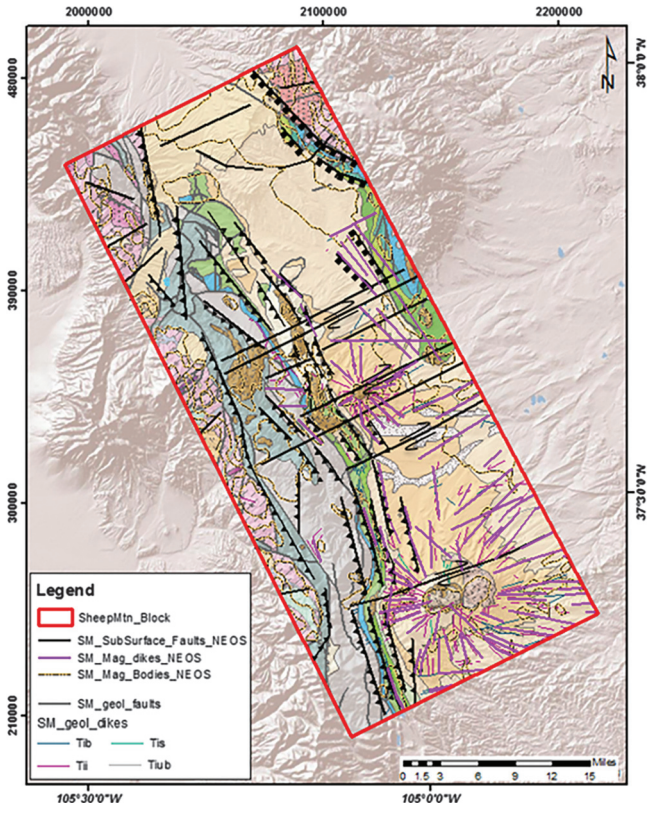

Figure 11. Geologic map from Figure 1 with interpreted faults, dikes, and intrusive bodies.

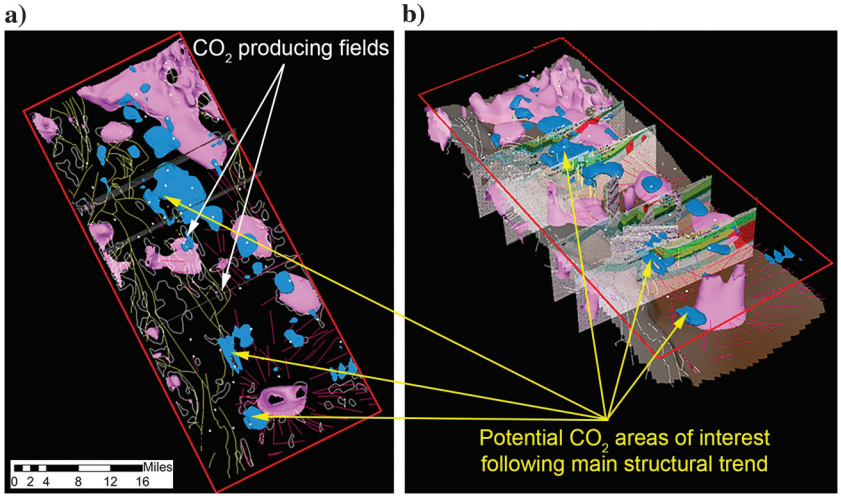

Figure 12. (a) Integrated map showing interpreted faults and dikes, some examples of 2D modeled sections, surface faults (white solid lines), surface dikes (solid red lines), high-susceptibility magnetic bodies (pink), and areas of resistivity less than 10 ohm-m (blue). (b) Integrated 3D geologic model including the same features as in (a), with added basement topography (brown surface). The areas identified by arrows are considered to have higher potential for CO_2 accumulation.

This approach allows us to predict areas where geologic and geophysical measurements, attributes and derivatives are similar to what is observed at a set of training locations and is useful in identifying patterns and relationships among the data sets that correlate with high-value exploration and production targets.

The training data used to build the similarity grid are comprised of known locations in the survey area that have desired characteristics indicative of CO_2 production (good producing wells), in addition to dry wells for CO_2. In this case, we selected as input grids, gravity, magnetic data, and corresponding first vertical derivatives, as well as grids of distance to interpreted features, such as faults.

We selected eight data layers as being relevant to the geology (Figure 13). These were used as input to the predictive analytics workflow. The geophysical data layers used included the CBG (mGal) (Figure 13a), first vertical derivative of CBG (mGal/ft) (Figure 13b), RTP magnetic field (nT) (Figure 13c), and first vertical derivative of RTP data (nT/ft) (Figure 13).

Based on our understanding of CO_2 reservoirs and their dependency on proximity to faults and igneous features, in addition to the geophysical data layers, we added a set of interpreted grids, representing the distance to various features. These grids included distance to major faults (Figure 13e), distance to intrusive volcanic bodies (Figure 13f), distance to dikes (Figure 13g), and distance to areas of resistivity less than 10 ohm-m (Figure 13h).

To assess CO_2 productivity, we built a map of similarity to the producing well locations and combined it with a map of dissimilarity to dry well locations (Figure 14a). High values (red) indicate a high similarity to producing well locations and a low similarity to dry well locations when looking at the set of eight input data layers. Conversely, low values (blue) indicate a high similarity to dry well locations and a low similarity to producing well locations.

The approach highlights several areas with CO_2 reservoir potential, in particular south of the known CO_2 fields, shown by producing well locations in Figure 14b, and north of the Sheep Mountain CO_2 field. The grids generated can be viewed as a proxy to the spatial distribution of CO_2 production away from the wells, using the selection of data layers. This selection is made based on our understanding of the data and the assumption that these specific layers have a complex underlying relation to the CO_2 production. Figure 14b shows the similarity grid overlain by the interpreted geologic features derived from our geophysical data analysis for reference. These mathematically derived results show high-similarity regions following the interpreted northwest–southeast structural trend, suggesting a strong relationship between CO_2 reservoirs and igneous intrusions along this structural trend.

The limited amount of production data coupled with the statistically and geographically nonrepresentative nature of the data presents challenges for any predictive technique. The results consequently must be carefully studied and the limitations kept in mind when

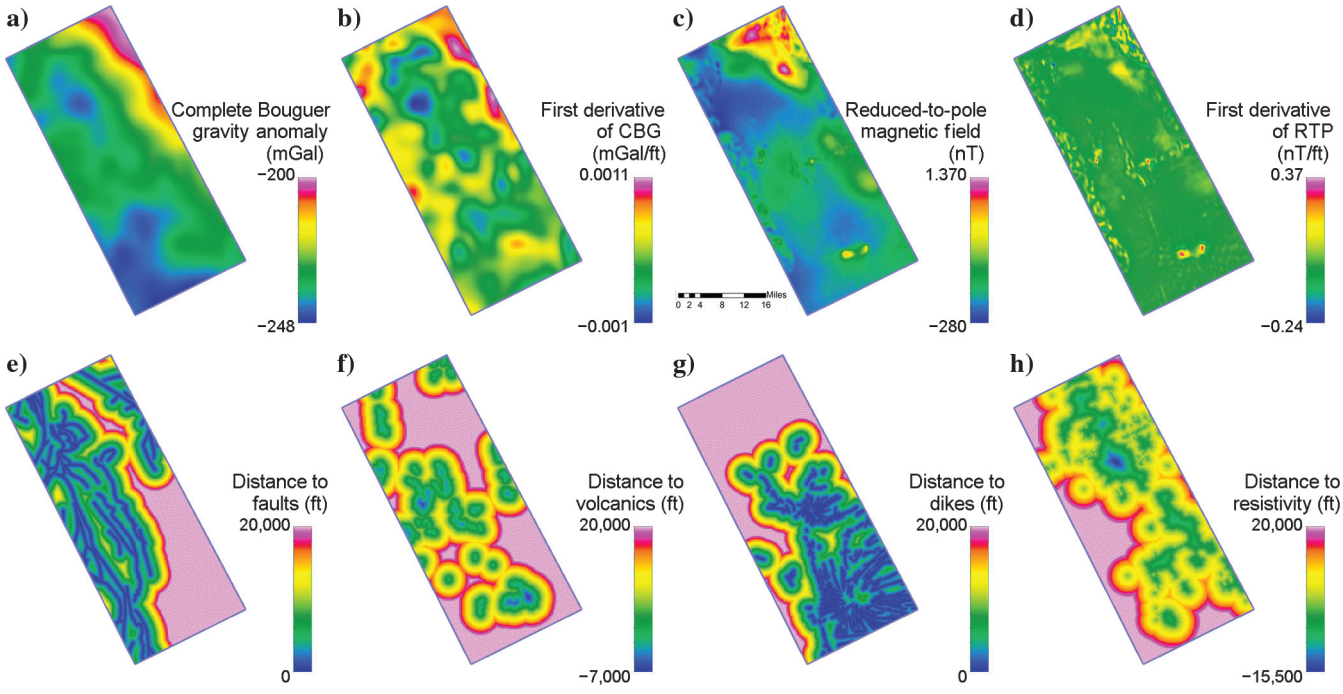

Figure 13. Predictive analytics grid inputs. (a) CBG, (b) first vertical derivative of CBG, (c) RTP magnetic field, (d) first vertical derivative of the RTP, (e) distance to major faults, (f) distance to intrusive bodies, (g) distance to dikes, and (h) and distance to areas of resistivity less than 10 ohm-m.

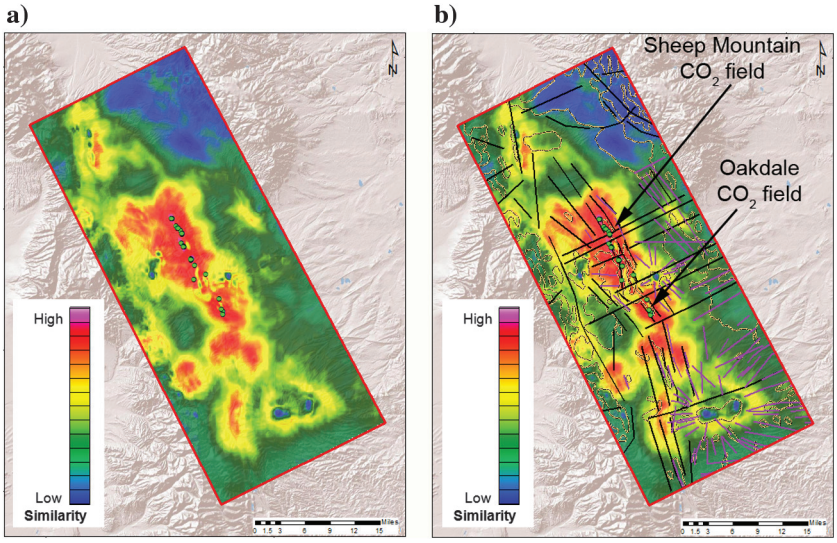

Figure 14. (a) Similarity maps from predictive analytics results using minimum distance methodology with producing wells (green) and (b) with interpreted faults (solid black lines), dikes (solid pink lines), and igneous bodies (orange lines).

drawing conclusions. Within a domain where the results are likely more stable, the approach indicates consistent areas of interest to the qualitative study, pointing to potential productive areas that warrant additional study and should be taken as guidance to the geologic understanding of the CO_2 field.

Conclusion

The overall outcome of this study demonstrates that integration of many interpretative products reveals a more robust exploration model that helps to delineate areas of higher CO_2 potential. With this methodology, we were able to better image and interpret igneous intrusions and faults not visible at the surface, which are key elements in the search for CO_2. We were able to recognize the main northwest–southeast structural trend of the basin from surface to depth by combining methodologies not used in the past. Additionally, we were also able to identify a perpendicular trend (northeast–southwest), not clearly visible at the surface, likely related to structures that may have developed during the evolution of faults associated with Precambrian suture zones. This integrated approach helped to identify two sedimentary subbasins separated by a structural high related to igneous intrusions, and determined the location of igneous intrusions and dikes. In the case of the dikes, we were also able to define their associated magnetic source bodies at depth. We were also able to model the topography of the Precambrian basement and approximate its unconformable contact to the overlying sedimentary basin.

Capitalizing on the geologic and geophysical knowledge of the data-rich areas in the Sheep Mountain and Oakdale CO_2 fields, we were able to extend investigations to the remainder of the study area and identify several prospective prime areas for CO_2 development. The integration of the interpretations from all data sets, predictive analytics results, and knowledge of CO_2 production, allowed us to delineate areas of interest for further exploration. The criteria for choosing these locations were based on the interpretation and knowledge of CO_2 production. There is a CO_2 trend that appears to be concentrated and bound by faults aligned with the major northwest–southeast structural trend. Transform faults associated with the northeast–southwest trend could be negative features in that they would allow CO_2 to escape to the surface, as observed on some dry wells drilled over the area, and should therefore be avoided. The proximity to intrusions and areas of low resistivity, and potentially low density, also appear to be associated with CO_2 reservoirs.

It has been demonstrated that the multiphysics acquisition and interpretation method we used contributes to improvement of the overall understanding of the study area. It also helps to identify regions with higher reservoir potential where seismic exploration alone is challenging due to complex geology, topographic relief, and permitting issues.

Acknowledgments

The authors would like to thank NEOS for allowing the publication of the results of this study, and Geotech Ltd. and Zonge International for collecting the EM data. The authors would also like to thank M. Baber, D. Chitwood, H. Huang, J. Livermore, S. Mazzoni, J. Poirier, and N. Skitt for their valuable contributions to this study.

References

Alumbaugh, D., H. Huang, J. Livermore, and M. S. Velasco, 2016, Resistivity imaging in a fold and thrust belt using ZTEM and sparse MT data: First Break, **34**, 65–72.

Auken, E., and A. Vest Christiansen, 2004, Layered and laterally constrained 2D inversion of resistivity data: Geophysics, **69**, 752–761, doi: 10.1190/1.1759461.

Ball, L. B., B. R. Bloss, P. A. Bedrosian, V. J. S. Grauch, and B. D. Smith, 2015, Airborne electromagnetic and magnetic survey data of the paradox and San Luis Valleys, Colorado: United States Geological Survey Open File Report 2015-1024.

Burchfiel, B. C., Z. Chen, K. V. Hodges, L. Yuping, L. H. Royden, D. Changrong, and X. Jiene, 1992, The south Tibetan detachment system, Himalayan orogen: Extension contemporaneous with and parallel to shortening in a collisional mountain belt: Geological Society of America.

Christiansen, R. L., and P. W. Lipman, 1972, Cenozoic volcanism and plate tectonic evolution of the western United States, II, Late Cenozoic: Philosophical Transactions of the Royal Society of London, **271-A**, 249–284, doi: 10.1098/rsta.1972.0009.

Clark, K. F., 1966, Geology of the Sangre de Cristo Mountains and adjacent areas, between Taos and Raton, New Mexico, *in* S. A. Northrop and C. B. Read, eds., Taos-Raton-Spanish Peaks Country (New Mexico and Colorado): Geological Society 17th Annual Fall Field Conference Guidebook, 56–65.

Cooper, M. A., and G. D. Williams, 1989, Inversion tectonics: Geological Society of London, Special Publications.

Eppink, J., T. L. Heidrick, R. Alvarado, and M. Marquis, 2014, Subsurface sources of CO_2 in the contiguous United States, Volume 1: Discovered reservoirs: Open-File Report 2014-1637, 89, U.S. Department of Energy (DOE) National Energy Technology Laboratory.

Geosoft, 2015a, Oasis Montaj, http://www.geosoft.com/products/oasis-montaj, accessed 15 March 2015.

Geosoft, 2015b, Geosoft, http://www.geosoft.com/, accessed 1 August 2015.

Geosoft, 2015c, Voxi Earth Modelling, http://www.geosoft.com/products/voxi-earth-modelling/, accessed 5 September 2015.

Gilfillan, S. M. V., C. J. Ballentine, G. Holland, B. Sherwood Lollar, S. Stevens, M. Schoell, and M. Cassidy, 2008, The noble gas geochemistry of natural CO_2 gas reservoirs from the Colorado plateau and rocky mountain provinces, USA: Geochimica et Cosmochimica Acta, **72**, 1174–1198, doi: 10.1016/j.gca.2007.10.009.

Johnson, R. B., 1968, Geology of the igneous rocks of the Spanish Peaks region, Colorado: Bulletin of the Geological Society of America, **47**, 1727–1784.

Johnson, C. M., 1991, Large-scale crust formation and lithosphere modification beneath middle to late Cenozoic calderas and volcanic fields, Western North America: Journal of Geophysical Research, **96**, 13485–13507, doi: 10.1029/91JB00304.

Jones, A. G., 2012, Distortion of magnetotelluric data: Its identification and removal, *in* A. D. Chave and A. G. Jones, eds., The magnetotelluric method theory and practice: Cambridge University Press, 219–302.

Karlstrom, K. E., and E. D. Humphreys, 1998, Persistent influence of Proterozoic accretionary boundaries in the tectonic evolution of southwestern North America: Interaction of cratonic grain and mantle modification events: Rocky Mountain Geology, **33**, 161–179, doi: 10.2113/33.2.161.

Key, K., 2012, Marine EM inversion using unstructured grids: A 2D parallel adaptive finite element algorithm: 82nd Annual International Meeting, SEG, Expanded Abstracts, doi: 10.1190/segam2012-1294.1.

Key, K., and C. Weiss, 2006, Adaptive finite-element modeling using unstructured grids: The 2D magnetotelluric example: Geophysics, **71**, no. 6, G291–G299, doi: 10.1190/1.2348091.

Kluth, C. F., 1986, Plate tectonics of the ancestral rocky mountains, in J. A. Peterson, ed., Paleotectonics and sedimentation, rocky mountain region, USA: AAPG Memoir, 353–369.

Kluth, C. F., and P. J. Coney, 1981, Plate tectonics of the Ancestral rocky mountains: Geology, **9**, 10–15, doi: 10.1130/0091-7613(1981)9<10:PTOTAR>2.0.CO;2.

Lindsey, D. A., B. J. Johnson, and P. A. M. Andriessen, 1983, Laramide and neogene structure of the Sangre de Cristo Range, south-central Colorado, *in* J. D. Lowell, ed., Rocky mountain foreland basins and uplifts: Rocky Mountain Association of Geologists, 219–228.

Lipman, P. W., 1984, The roots of ash flow calderas in Western North America: Windows into the tops of granitic batholiths: Journal of Geophysical Research, **89**, 8801–8841, doi: 10.1029/JB089iB10p08801.

Lipman, P. W., H. J. Prostka, and R. L. Christiansen, 1972, Cenozoic volcanism and plate tectonic evolution of the western United States, I, Early and Middle Cenozoic: Philosophical Transactions of the Royal Society of London, **271-A**, 217–248, doi: 10.1098/rsta.1972.0008.

Lo, B., J. M. Legault, P. Kuzmin, and M. Combrink, 2009, ZTEM (airborne AFMAG) tests over unconformity uranium deposits: 20th Australian Society of Exploration Geophysicists International Conference and Exhibition, Extended Abstracts, 4.

Lo, B., and M. Zhang, 2008, Numerical modeling of Z-TEM (airborne AFMAG) responses to guide exploration strategies: 78th Annual International Meeting, SEG, Expanded Abstracts, 1098–1102.

Marshak, S., K. Karlstrom, and J. Timmons, 2000, Inversion of Proterozoic extensional faults: An explanation for the pattern of Laramide and Ancestral Rockies intracratonic deformation, United States: Geology, **28**, 735–738, doi: 10.1130/0091-7613(2000)28<735:IOPEFA>2.0.CO;2.

Merin, I. S., J. R. Everett, and P. R. Rose, 1988, Tectonic evolution and structural geology of the Raton Basin, Colorado and New Mexico, and Huerfano Park, Colorado, *in* L. L. Sloss, ed., Sedimentary cover — North American Craton: U.S.: Geological Society of America, Geology of North America, 170–179.

Mutschler, F. E., E. E. Larson, and R. M. Bruce, 1988, Laramide and younger magmatism in Colorado: New petrologic and tectonic variations on old themes: Colorado School of Mines Q, **82**, 1–47.

Northrop, S. A., H. H. Sullwold, Jr., A. J. MacAlpin, and C. P. Rogers, 1946, Geologic maps of a part of the Las Vegas Basin and of the foothills of the Sangre de Cristo Mountains, San Miguel and Mora Counties, New Mexico: United States Geological Survey Oil and Gas Investigations Preliminary Map OM-0054, scale 1:190, 000.

Penn, B. S., 1994, An investigation of the temporal and geochemical characteristics, and the petrogenetic origins of the Spanish Peaks intrusive rocks of south-central Colorado: Ph.D. dissertation, Colorado School of Mines.

Penn, B. S., and D. A. Lindsey, 2009, 39Ar/40Ar dates for the Spanish Peaks intrusions in south-central Colorado: Rocky Mountain Geology, **44**, 17–32, doi: 10.2113/gsrocky.44.1.17.

Penn, B. S., R. F. Wendlandt, E. C. Simmons, L. W. Snee, and D. M. Unruh, 1994, Geochemical evolution of the Spanish Peaks intrusive rocks of south-central Colorado: Geological Society of America Meeting, Abstracts, 58.

Popov, M., V. Nuccio, T. Dyman, T. Gognat, R. Johnson, J. Schmoker, M. Wilson, and C. Bartberger, 2001, Basin-centered gas systems of the U.S.: United States Geological Survey open-file report 01-135, version 1.0.

Ruleman, C., and M. Machette, 2007, An overview of the Sangre de Cristo fault system and new insights to interactions between quaternary faults in the Northern Rio Grande Rift: USGS open file 07-1193, Ch. J.

Sims, P., V. Bankey, and C. Finn, 2001, Preliminary precambrian basement map of Colorado, a geological interpretation of the Aeromagnetic anomaly map: USGS open-file report 01–364.

SRTM, 2000, Shuttle radar topography mission (SRTM) 1 arc-second global, https://lta.cr.usgs.gov/SRTM1Arc, accessed 1 March 2015.

Stevens, S. H., T. E. Lombardi, B. Kelso, and J. M. Coates, 1992, A geologic assessment of natural gas from coal seams in the Raton and Vermejo Formations, Raton Basin: Topical report prepared for the Gas Resource Institute under contract no. 5091-214-2316, GRI 92/0345, 84, Advanced Resource International Inc.

Talwani, M., J. L. Worzel, and M. Landisman, 1959, Rapid gravity computations for two-dimensional bodies with application to the Mendocino submarine fracture zone: Journal of Geophysical Research, **64**, 49–59, doi: 10.1029/JZ064i001p00049.

Talwani, M., and J. R. Heirtzler, 1964, Computation of magnetic anomalies caused by two-dimensional bodies of arbitrary shape, *in* G. A. Parks, ed., Computers in mineral industries. Part 1: Stanford University of Publication, Geological Sciences, 464–480.

Telford, W. M., L. P. Geldart, and R. E. Sheriff, 1990, Applied geophysics, 2nd ed.: Cambridge University Press.

USGS, 2005, National Assessment of Oil and Gas Project — Raton Basin-Sierra Grande Uplift Province (041) Boundary, http://pubs.usgs.gov/dds/dds-069/dds-069-n/SPATIAL/doc/pr41bndg.htm, accessed 25 May 2015.

UTEP, 2008, Gravity and magnetic extract utility, http://irpsrvgis08.utep.edu/viewers/Flex/GravityMagnetic/GravityMagnetic_CyberShare/, accessed 1 March 2015.

Weidelt, P., and A. D. Chave, 2012, The magnetotelluric response function, *in* A. D. Chave and A. G. Jones, eds., The magnetotelluric method theory and practice: Cambridge University Press, 122–164.

Williams, J. M., and B. D. Rodriguez, 2007, Magnetotelluric data, Southern San Luis Valley, Colorado: USGS open file report 2007-1291.

Maria Soledad Velasco received an undergraduate degree in earth sciences from the Universidad de Buenos Aires, Argentina; an M.S. in geosciences from the University of Memphis, TN; and a Ph.D. in geosciences from the University of Arizona. She is a geoscientist with more than 13 years of experience working on exploration projects in onshore and offshore conventional and unconventional basins around the world, specializing in geologic and geophysical data integration and reservoir characterization in large- and small-scale tectonic settings, working for Fugro, Chevron, ConocoPhillips, BP, and NEOS. Her early career focused on mapping the western part of Argentina working for the Servicio Geologico Minero Argentino creating structural and stratigraphic maps for oil and gas and mining industries. While working for Fugro in California and Texas, part of her work also included seismic acquisition offshore Gulf of Mexico and Brazil. Her current position at NEOS includes leading exploration projects in North America, Eurasia, and South America. Her technical interests include the application of new technology and the integration of geologic and geophysical methods to understand complicated tectonic environments.

David Alumbaugh did undergraduate work that was followed by graduate work in EM geophysics at UC Berkeley, and his first postgraduate job was at Sandia National Laboratories in Albuquerque, New Mexico, where he architected one of the first 3D EM forward-modeling and inversion algorithms that made use of massively parallel computing platforms. He was raised in Southern California. His interest in earth science was sparked by a childhood fascination with volcanoes and earthquakes. In the late 1970s, as he was finishing high school, oil prices spiked and a local newspaper published a list of promising future careers, with "geologist" near the top. This event coupled with the childhood fascination with geologic processes led him to pursue an undergraduate degree in geological sciences at San Diego State, where he took a keen interest in EM geophysical methods. After a four-year stint as a professor in the geological engineering Program at the University of Wisconsin, he and his family returned to Berkeley, California, where he took a position at Schlumberger's EMI Technology Center, where his work focused on commercializing his Ph.D. work in cross-well EM imaging and developing an intellectual technology portfolio for marine CSEM. Since leaving Schlumberger for Chevron and most recently NEOS, his work has continued to focus on the incorporation of EM geophysical techniques into exploration workflows, as well as advancing physics, and to a lesser extent, statistically based methods of fusing multiphysics data into geologic interpretations.

Emmanuel Schnetzler received an undergraduate degree in mathematics and physics in his hometown of Strasbourg. Later, he was accepted at the Ecole Nationale Supérieure de Géologie, where he developed a strong interest in computers and programming, and he had an opportunity to apply to computer geology as part of the original team developing the reservoir modeling software Gocad. He has been rock hounding since his early teens, collecting fossils and minerals from his local area of Alsace and on family trips across Europe, encouraged by his geologist uncle. A couple of summer internships with Elf Aquitaine (now Total) exposed him to geostatistics and led him to continue in this specialization at Stanford University. His fist job brought him to Norway with Odin (now Roxar), where he had a chance to assume multiple roles with a small company, being involved in software development, project work, and training in geostatistics as well as on software. He returned to the United States in 1997 to pursue a consulting carrier, working with a variety of oil and gas and mining companies, including Shell, Statoil, Chevron, ExxonMobil, and BHP Billiton. At the same time, he cofounded Statios to develop and commercialize geostatistical software and teach courses. His work at NEOS allows him to explore multivariate statistical and machine learning techniques and develop workflows applied to oil and gas and mining problems. His involvement with projects allows him to strive for practical solutions to concrete situations. He enjoys his interactions with team members and the constant opportunity of learning from specialists in different disciplines.